PHYSICS

Ultrabroadband photosensitivity from visible to terahertz at room temperature

Dong Wu[1]*, Yongchang Ma[2], Yingying Niu[3], Qiaomei Liu[1], Tao Dong[1], Sijie Zhang[1], Jiasen Niu[1], Huibin Zhou[1], Jian Wei[1], Yingxin Wang[3], Ziran Zhao[3], Nanlin Wang[1]*

Charge density wave (CDW) is one of the most fundamental quantum phenomena in solids. Different from ordinary metals in which only single-particle excitations exist, CDW also has collective excitations and can carry electric current in a collective fashion. Manipulating this collective condensation for applications has long been a goal in the condensed matter and materials community. We show that the CDW system of 1T-TaS_2 is highly sensitive to light directly from visible down to terahertz, with current responsivities on the order of ~1 AW^{-1} at room temperature. Our findings open a new avenue for realizing uncooled, ultrabroadband, and sensitive photoelectronics continuously down to the terahertz spectral range.

INTRODUCTION

The ability to convert light into electronic signal is critical in photoelectronics. The effect has broad applications ranging from imaging, communication, quantum information to space science. However, high sensitivity to light over a broad spectral range, especially in low frequencies down to terahertz (THz) at room temperature (RT), is particularly rare but meritorious. Conventional semiconductors, such as silicon, gain the photoresponse properties through the single-particle excitations across the band gap and are transparent to the energy below the gap to THz photons (*1*–*4*). On the other hand, the photoresponse properties of simple metals or very narrow-gap semiconductors suffer seriously from free-carrier screening and fast-quenching effect, especially at elevated temperatures (*4*, *5*). Solids with collective electronic states (*6*, *7*), on the contrary, can have an electronic response in a collective fashion and behave quite differently from the single-particle excitations.

Charge density wave (CDW) is one of the most studied collective electronic states in solids. Different from ordinary metals in which only single-particle excitations exist, CDW materials also have collective excitations being referred to as an amplitude mode and a phase mode. Amplitude excitation behaves as optical phonons and is not expected to have a direct effect on the electric transport properties, while phase excitation corresponds to the translational motion of the CDW condensate and can have a marked effect on charge transport properties. The phase mode is usually pinned at finite frequency. By applying a dc electric field, the phase mode can be driven into a current-carrying state being usually referred to as sliding CDW, leading to nonlinear current-voltage (*I*-*V*) characteristics (*6*, *7*). As a result, the frequency- and electric field–dependent conduction exhibits characteristic features of the translational motion of the CDW condensate. Here, we show that incident illuminations can induce significant changes in the electronic properties of 1T-TaS_2, a well-known two-dimensional (2D) CDW compound, making it a superior system for realizing high-sensitive photoelectronics directly in an ultrabroadband range from visible (Vis) to infrared (IR) and even THz at RT.

[1]International Center for Quantum Materials, School of Physics, Peking University, Beijing 100871, China. [2]School of Materials Science and Engineering, Tianjin University of Technology, Tianjin 300384, China. [3]Key Laboratory of Particle and Radiation Imaging, Department of Engineering Physics, Tsinghua University, Beijing 100084, China.
*Corresponding author. Email: dongwu@pku.edu.cn (D.W.); nlwang@pku.edu.cn (N.W.)

1T-TaS_2 has a crystalline structure consisting of planes of hexagonally arranged tantalum atoms sandwiched by two layers of sulfur atoms, as shown in Fig. 1A. As one of the most studied CDW compounds of 2D transition metal chalcogenides, 1T-TaS_2 hosts multiple equilibrium states arising from the interplay between electron correlation, lattice strain, and Fermi surface nesting (*8*–*13*). Upon cooling across ~550 K, the system transfers from a simple metal into an incommensurate (IC)–CDW state, with an associated modulations of lattice distortions. The distortions sharpen to form star-shaped polaron clusters (see inset of Fig. 1B) and become nearly commensurate (NC) below T_c = 350 K, being referred to as the phase of NC-CDW. Further cooling leads to another first-order phase transition near 183 K, below which the system becomes a gapped commensurate (C)–CDW state. These variations have made 1T-TaS_2 an ideal playground for investigating CDW dynamics (*12*, *13*) and novel metastable states (*14*, *15*) via external manipulations.

RESULTS

High-quality single crystals of 1T-TaS_2 were synthesized by chemical vapor transport (CVT) method in a sealed quartz tube, with a subsequent quenching process to retain the 1T phase (see figs. S1 to S3 for more information). Figure 1B shows the temperature-dependent resistivity of our 1T-TaS_2 sample, which captures the CDW phases upon cooling from 400 K. Above the critical temperature T_{c1} = 350 K, the resistivity keeps almost a constant value. Then, it undergoes an abrupt jump at T_{c1}, reflecting a phase transition from IC-CDW to NC-CDW (*13*, *15*). Near RT, the resistivity values have the order of 1 mohm·cm, where the values are close to the maximum universal values predicted in the 2D metals (*16*, *17*). Different from the IC-CDW phase, the ρ-*T* curve in the NC-CDW phase has an abnormal negative slope. Upon further cooling down to 183 K, the resistivity shows another abrupt upward jump, corresponding to the formation of the C-CDW state. A significant hysteresis is seen between cooling down and warming up the sample, reflecting the first-order phase transition.

Two-terminal devices are used to investigate the photoactive electric properties of the NC-CDW phase of 1T-TaS_2 at RT. The prototype devices are fabricated on exfoliated thin flakes in thickness of several micrometers with the gold electrodes prepared by deposition method. Then, the flakes are cut into slim channels and transferred onto sapphire substrates for using as devices. The resultant structure is depicted in Fig. 1C. A 1T-TaS_2 device with the channel (length, 780 μm;

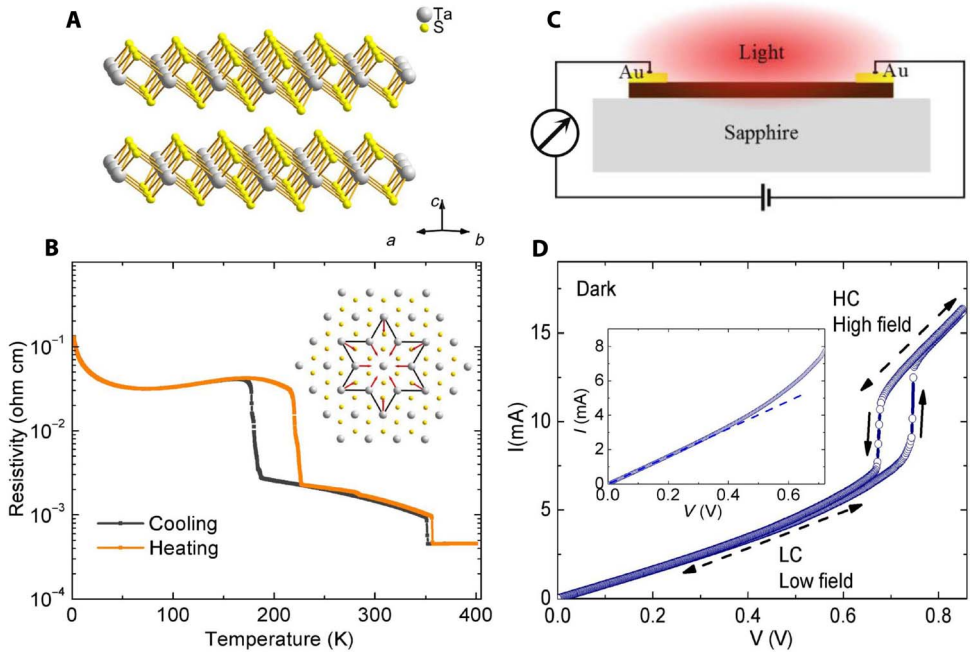

Fig. 1. RT NC-CDW phase in 1T-TaS_2 and its electronic properties. (**A**) Schematic images of layered structure. (**B**) Temperature dependence of the four-probe resistivity on temperature cycling. The inset depicts the lattice distortions associated with NC-CDW phase. (**C**) Schematic of the two-terminal device used for photoresponse characterization. (**D**) The *I-V* curve under dark for the two-terminal device measured under voltage sweep up and down modes at RT. The abrupt switching between LC and HC states can be driven by the applied bias. The inset shows the quasi-linear *I-V* at low fields (the blue dashed is a guideline) and a nonlinear behavior at the relative high fields.

width, 23 μm) between the electrodes is used for illustrating our results. The representative *I-V* curves measured at RT under dark are plotted in Fig. 1D for both sweeping up and down modes. Both curves can be divided into three different intervals: a linear section at low electric fields, a nonlinear section followed by a current jump-up, and a high-conduction (HC) section thereafter. The conductivity value at high-field ends is close to that measured in IC-CDW state. Previously, it has been revealed for a field-driven switching in *I-V* (below 180 K) characterizing a phase transition from C-CDW to IC-CDW in the 1T-TaS_2 system (*13*). By analogous considerations, the observed switching in *I-V* at RT might represent the phase transition from NC-CDW to IC-CDW. A more plausible mechanism responsible for this switching character relates to CDW sliding dynamics driven by the applied electric field (*6*, *8*). Below the sliding threshold voltage V_T, the CDW condensate is primarily pinned to the background lattice. While near V_T, a significant nonlinear *I-V* interval emerges, corresponding well to the depinning of CDW condensate transport. These electric field–sensitive characteristics have been widely observed and investigated in traditional CDW materials, such as $NbSe_3$, TaS_3, and molybdenum blue bronzes (*18*–*21*). As a result, in the 1T-TaS_2 device, the conduction phase changing between low-conduction (LC) and (HC) states is manifested (Fig. 1D).

Unlike usual semiconductor, which is transparent below the band energy gap, an 1T-TaS_2 crystal has rather high in-plane reflectivity (R) at low energy. Figure 2A shows the value of $1 - R$ as a function of wavelength from Vis down to THz region at RT, which roughly reflects the absorption of the crystal sample. The penetration depths are estimated to be in the range between ~40 nm (at $\lambda = 1$ μm) in near-IR and ~0.6 μm (at $\lambda = 100$ μm) in THz at RT, respectively (see Materials and Methods). When illuminating, the *I-V* function of 1T-TaS_2 devices was found to be reshaped. Figure 2B depicts such a typical current response for a laser illumination of $\lambda = 1550$ nm. As seen in the figure, the whole *I-V* curve under illumination is lifted above the dark one. The current response is relatively weak at low biases, but it gets more and more drastic as the applied biases increase into the nonlinear interval approaching the switching edge. These effects can be characterized as the direct photoresponse of the 1T-TaS_2 material, without competitive influence from the contacts. The current response increases with increasing light intensity, accompanied by a gradual reduction of the transition edges (see fig. S4 for more information). The threshold V_T exhibits a quasi-linear relationship with the incident intensity (Fig. 2C), suggesting that the CDW pinning force can be tuned by the illumination fluences.

Figure 2D illustrates the current switching effects when a constant illuminating intensity is turned on and off. Away from the threshold voltage (for instance, at the bias voltage of 0.71 V; Fig. 2D, left), stable photocurrent switching is recorded as the illumination is modulated by a shutter. When the light intensity is high enough, it will drive the shifted switching edge completely into the fields below the initial threshold voltage V_T, giving rise to a bias window connecting the LC with HC states (see Fig. 2B). Comparatively, for the applied potential located inside the bias window (for example, at 0.73 V), a large photoeffect corresponding to the conduction state transition from LC to HC state could be induced (Fig. 2D, right), indicating that photoexcitation could be an efficient method to control the dynamical CDW phases in 1T-TaS_2.

For a given applied voltage below V_T, upon increasing the incident intensity, the current also shows a critical intensity P_c in *I-P* function (where P is the incident intensity), as shown in Fig. 3A. Below P_c, the corresponding *I-P* curve demonstrates a quasi-linear behavior. The range of the linear photoresponse region depends strongly on the applied bias. As the intensity increases, the current response jumps to a

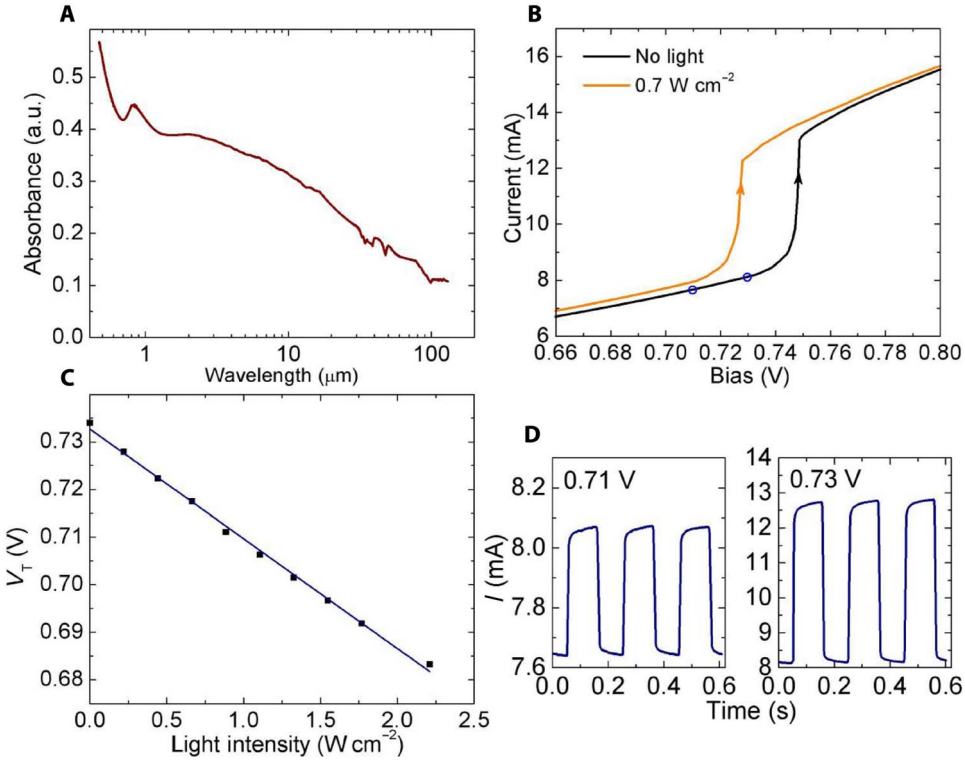

Fig. 2. Absorbance spectra and electrical response under illuminations. (**A**) In-plane optical absorbance spectrum of freshly cleaved surface of 1T-TaS_2 crystal samples. a.u., arbitrary units. (**B**) The photoresponse of dc electrical current of a device for voltage sweep up mode. The light intensity is 0.7 W cm^{-2}. (**C**) The threshold voltage V_T changes linearly with the incident light intensity. (**D**) Current switching effects for applied bias 0.71 V (left) and 0.73 V (right), as bias values are marked out as blue circles in (B). For the experiment, the illumination (0.7 W cm^{-2}) is chopped at a frequency of 5 Hz. The illuminations were provided by a continuous-wave solid-state laser at λ = 1550 nm, with a laser spot of ~2.7 mm in diameter focusing on the device.

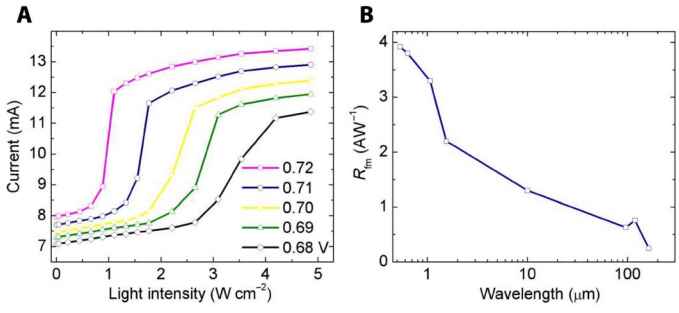

Fig. 3. The Uultrabroadband photoresponse. (**A**) The current response as the function of incident intensities was investigated at illumination of λ = 1550 nm for applied voltages below the initial threshold of dark. For relatively weak illuminations, a linear relationship for the current with incident intensity can be established. While for intense illuminations, the conduction transition of LC-HC can be achieved. (**B**) The ultrabroadband photoresponsivity measured at external bias 0.72 V. The illuminations were provided by continuous-wave solid-state lasers from Vis to THz at λ = 532, 635, 1064, and 1550 nm and λ = 10, 96.3, 118.8, and 163 μm, respectively (see Materials and Methods).

higher value corresponding to a higher constant conductance, indicating that the LC-HC state transition is triggered.

Surprisingly, ultrabroadband photosensitivity, similar to the aforementioned photoresponse effects, is observed at wavelengths ranging from Vis down to THz at RT in the 1T-TaS_2 device (see fig. S6 for more information). As for intensive illuminations, the LC-HC conduction phase transition can be induced. For weak illuminations, the *I-P* function keeps in a quasi-linear behavior that the ratio of I_p/P manifests independently on the incident power, where I_p is the net photocurrent, being defined as the photoexcited current minus the dark current. We numerically investigate such a nominal current responsivity, $R_{fm} = I_p/P$, where the R_{fm} figure-of-merit quantifies the signal component of the sensitivity and is important to photodetection applications (*5*). As shown in Fig. 3B, high current responsivities are recorded by adjusting the applied potentials approaching V_T, with the magnitude between 0.25 and 3.92 AW^{-1} being obtained at bias voltage of 0.72 V for an instance (see fig. S7 for more information). At THz wavelength λ = 118.8 μm, the responsivity is 0.76 AW^{-1}, which is about two orders of magnitude higher than that detected in graphene-based ultrabroadband and THz detector systems (see table S1 for more information) (*22*). To the best of our knowledge, few materials were reported to demonstrate potentials for such direct ultrabroadband down to a THz photoresponse, as referring to graphene, topological insulators, and recently a telluride of $EuSbTe_3$ (*22*–*24*). Compared with them, 1T-TaS_2 is the system presenting exceptionally strong photoresponse, which is likely to be related to the complex CDW dynamics, showing that significant potentials of RT photodetection across the wavelengths range continuously from Vis to THz regimes.

To facilitate the applications, we analyzed the noise spectra of the device as a function of frequency (*25*). It manifests a structureless broadband noise in $1/f^{\alpha}$ at low frequencies, which approaches the Johnson-Nyquist noise limit at higher frequencies. We calculate the noise equivalent power (NEP), that is, the signal power when the signal-to-noise ratio

is unity (*5*). Operating basically at electric fields with linear photoresponse, the named NEP is evaluated to be ~80 pW $Hz^{-1/2}$ at λ = 532 nm for the applied bias 0.71 V (see fig. S8 for more information). At THz frequencies, the available NEP of ~0.4 nW $Hz^{-1/2}$ (at λ = 118.8 μm) rivals the state-of-art RT THz detectors such as thermal bolometers and Golay cells (*26*).

It is important to characterize the time scale of the photoresponse effect. It appears that the intrinsic photoresponse time scale cannot be correctly measured by using a normal shutter or a mechanical chopper with low-frequency modulation since the photoresponse is too fast. We used a pulse femtosecond laser with a regenerate amplifier and an optical parametric amplifier, with a repetition rate of 1 kHz to investigate the photoresponse of 1T-TaS_2 devices at RT. The temporal "time-of-flight" response (*27*, *28*) by the photoexcitations under applied bias voltage is recorded by an oscilloscope with a bandwidth of 350 MHz, for which a channel with 50-nm thickness and 30-μm length between the electrodes is used for measurement. The result is shown in Fig. 4. The pulsed current signal rises up immediately after the photoexcitation. The rising time is recorded to be ~1.5 ns, which is still limited by the time resolution of the oscilloscope electronics. The photoexcited signal shows approximately a plateau below 30 ns and then falls fast in another 30 ns, followed by a rather slow tail. The rather long-lasting period of the plateau indicates that the sample is driven to a metastable state, which can be considered as a local variation of the CDW phase (*14*, *15*, *29*). The slow tail is bias-dependent, which might be related to the defects and external stress (*15*). The photoresponse can be hardly detected when the applied bias exceeds the threshold voltage V_T (see fig. S9 for more information). The results suggest that the experimental observations can be attributed to the NC-CDW dynamical photoresponse.

CONCLUSIONS

To summarize, we have demonstrated that the layered 2D CDW system 1T-TaS_2 is highly sensitive to light at RT with ultrabroadband photoresponse from Vis to THz spectral range. The revealed characters have direct relations with the inherent collective electronic dynamics of the CDW state, and the results may extend well beyond the 1T-TaS_2 material case. The advantages of uncooled and ultrabroadband photoresponse make this 2D chalcogenide highly attractive for exploring more efficient photoelectronics, such as novel memory devices, photodetectors, and spectroscopy, from both experimental and theoretical perspectives.

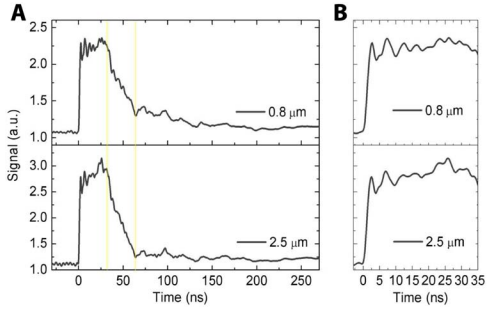

Fig. 4. Temporal photoresponse studied by pulse excitations. (**A**) Rise and fall edges showing fast and slow components. The yellow lines are guides identifying three different relaxation processes including a short retention of ~30 ns, a fast fall in another 30 ns, and a slow tail. The small superimposed oscillations are due to ringing of the circuit. (**B**) Close-up views of the fast components of the rise edges and short retention. The rise time shorter than 2 ns can be recognized, and the accurate rise time analysis is out of the limitation of our oscilloscope. Here, in the experiments, the pulsed femtosecond lasers are provided at wavelengths λ = 0.8 μm (~100 fs, 1.2 mJ cm^{-2}) and λ = 2.5 μm (~150 fs, 1 mJ cm^{-2}), with the repetition rate of 1 kHz.

MATERIALS AND METHODS

Sample preparation

1T-TaS_2 single crystals were grown by the CVT method with iodine as a transport agent. The high-purity Ta (4N) and S (4N) were mixed in chemical stoichiometry with additional iodine (~2% total mass) and heated at 850°C for 2 days in an evacuated quartz tube. Then, the quartz tube was transferred to a two-zone furnace, where the source zone and growth zone were fixed at 880° and 780°C for 2 weeks. The tube was then quenched in cold water to retain the 1T phase. The process yielded large shining crystal plates with a common size of ~3 mm × 3 mm.

For device preparation, thin flakes were exfoliated from the bulk crystals by the scotch tape method. Two-terminal electrodes were prepared with the gold deposition method on the flakes. The flakes were then cut into slim bars. The devices with different dimensions were checked for photoresponse properties, and they showed analogous response features.

Optical spectral properties

For optical spectra analysis, the near-normal incident reflectance spectra were measured on freshly cleaved 1T-TaS2 bulk plates (thickness, ~50 μm) by a Bruker 80v/S spectrometer in the 50- to 24,000-cm^{-1} frequency range. An in situ overcoating technique was used for reflectance measurements (*30*). The penetration depth δ_0 is estimated by $1/\delta_0 = 4\pi\omega k/c$, where k is the extinction coefficient that is available from the reflectivity spectrum by Kramers-Kronig transformation. The penetration depths were evaluated to be far smaller than 0.5 μm from ultraviolet to THz at RT (for instance, it is ~45 nm at λ = 1 μm and ~0.6 μm at λ = 100 μm, respectively). Thus, the absorbance spectrum applied to the thick samples (that is, several micrometers) can be roughly evaluated by $\alpha = 1 - R$, where α is the absorbance and R is the reflectance.

Electrical and photoresponse properties

The dc electrical signals were measured using a Keithley 2602B sourceMeter. For photocurrent measurements, various continuous-wave lasers were used as light sources, as referred to the solid-state lasers (λ = 532, 635, 1064, and 1550 nm) and mid-IR source (10 μm, CO_2 laser). A far-IR gas laser (FIRL-100, Edinburgh Instruments Ltd.) served as the THz illumination source (163, 118.8, and 96.5 μm). The incident power was monitored by calibrated power meters. The continuous-wave lasers combined with a shutter were used to test the current switching effect.

The absolute responsivity was calculated by

$$R_{fm} = (I_{on} - I_{dark})/P$$

where R_{fm} is in units of AW^{-1}, I_{on} is the current under illumination, I_{dark} is the dark current, and P is the incident light power.

The NEP was estimated by NEP = I_n/R_{fm}, where I_n is the noise current in A $Hz^{-1/2}$, R_{fm} is the responsivity in units of AW^{-1}, and NEP is in units of W $Hz^{-1/2}$. For evaluating NEP values, the noise current was

extracted from the noise power spectra at a frequency bandwidth of 50 Hz, and the photoresponsivities were estimated at the same frequency.

The noise power spectra were measured using homemade amplifiers and then digitized with a data acquisition card. A cross-correlation algorithm was used to average out the instrument noise. Only battery and ballast resistors were used to avoid extra noises due to an external circuit. The device was kept in a shielded dark enclosure.

For temporal photoresponse analyses, pulsed femtosecond lasers at wavelengths $\lambda = 800$ nm (100 fs, 1.2 mW cm^{-2}) and $\lambda = 2.5$ μm (150 fs, 1 mW cm^{-2}) with the repetition rate of 1 kHz were provided as laser sources. The temporal electrical signals were recorded by an oscilloscope (the bandwidth is 350 MHz; DSO-X 3034A, Agilent Technologies).

SUPPLEMENTARY MATERIALS

Supplementary material for this article is available at http://advances.sciencemag.org/cgi/content/full/4/8/eaao3057/DC1

Materials characterization

Photoresponse spectra as the function of applied bias and incident intensity

Estimation of the temperature rise

THz response characterization

Ultrabroadband photoresponsivity operating at quasi-linear photoresponse conditions

Noise characteristics of 1T-TaS_2 devices

Temporal response of the device after the femtosecond pulse excitations

Fig. S1. Energy dispersive spectrum analysis of the 1T-TaS_2 as-grown crystals.

Fig. S2. In-plane IR spectra of the 1T-TaS_2 measured at 300 and 78 K.

Fig. S3. Optical images of 1T-TaS_2 as-growth crystals and devices.

Fig. S4. *I-V* characteristics of the device as the function of applied bias and incident intensity.

Fig. S5. The estimated steady-state value of temperature rises for the illumination of ~1 W cm^{-2} at various wavelengths in our measurement range for a sample with the dimension ~ 780 μm × 23 μm × 6 μm.

Fig. S6. THz response characterizations at $\lambda = 118.8$ μm.

Fig. S7. Ultrabroadband photosensitivity operating at quasi-linear photoresponse conditions.

Fig. S8. Noise current analysis for the 1T-TaS_2 device at external bias 0.71 V.

Fig. S9. Temporal response of the device after the 150-fs pulse excitations.

Table S1. Parameters for 1T-TaS_2, graphene, and topological insulator–based photodetectors.

References (*31*–*38*)

REFERENCES AND NOTES

1. R. A. Soref, Silicon-based optoelectronics. *Proc. IEEE* **81**, 1687–1706 (1993).
2. R. Ciupa, A. Rogalski, Performance limitations of photon and thermal infrared detectors. *Opto-Electron. Rev.* **5**, 257–266 (1997).
3. V. Adinolfi, E. H. Sargent, Photovoltage field-effect transistors. *Nature* **542**, 324–327 (2017).
4. M. Tonouchi, Cutting-edge terahertz technology. *Nat. Photonics* **1**, 97–105 (2007).
5. F. H. L. Koppens, T. Mueller, Ph. Avouris, A. C. Ferrari, M. S. Vitiello, M. Polini, Photodetectors based on graphene, other two-dimensional materials and hybrid systems. *Nat. Nanotechnol.* **9**, 780–793 (2014).
6. G. Grüner, The dynamics of charge-density waves. *Rev. Mod. Phys.* **60**, 1129–1181 (1988).
7. H. Fröhlich, On the theory of superconductivity: The one-dimensional case. *Proc. R. Soc. A* **223**, 296–305 (1954).
8. P. Monceau, Electronic crystals: An experimental overview. *Adv. Phys.* **61**, 325–581 (2012).
9. B. Sipos, A. F. Kusmartseva, A. Akrap, H. Berger, L. Forró, E. Tutiš, From Mott state to superconductivity in 1T-TaS_2. *Nat. Mater.* **7**, 960–965 (2008).
10. L. Perfetti, P. A. Loukakos, M. Lisowski, U. Bovensiepen, M. Wolf, H. Berger, S. Biermann, A. Georges, Femtosecond dynamics of electronic states in the Mott insulator 1T-TaS_2 by time resolved photoelectron spectroscopy. *New J. Phys.* **10**, 053019 (2008).
11. A. W. Tsen, R. Hovden, D. Wang, Y. D. Kim, J. Okamoto, K. A. Spoth, Y. Liu, W. Lu, Y. Sun, J. C. Hone, L. F. Kourkoutis, P. Kim, A. N. Pasupathy, Structure and control of charge density waves in two-dimensional 1*T*-TaS_2. *Proc. Natl. Acad. Sci. U.S.A.* **112**, 15054–15059 (2015).
12. T. Ishiguro, H. Sato, Electron microscopy of phase transformations in 1*T*-TaS_2. *Phys. Rev. B* **44**, 2046–2060 (1991).
13. M. J. Hollander, Y. Liu, W.-J. Lu, L.-J. Li, Y.-P. Sun, J. A. Robinson, S. Datta, Electrically driven reversible insulator–metal phase transition in 1T-TaS_2. *Nano Lett.* **15**, 1861–1866 (2015).
14. L. Stojchevska, I. Vaskivskyi, T. Mertelj, P. Kusar, D. Svetin, S. Brazovskii, D. Mihailovic, Ultrafast switching to a stable hidden quantum state in an electronic crystal. *Science* **344**, 177–180 (2014).
15. I. Vaskivskyi, J. Gospodaric, S. Brazovskii, D. Svetin, P. Sutar, E. Goreshnik, I. A. Mihailovic, T. Mertelj, D. Mihailovic, Controlling the metal-to-insulator relaxation of the metastable hidden quantum state in 1*T*-TaS_2. *Sci. Adv.* **1**, e1500168 (2015).
16. P. Fazekas, E. Tosatti, Electrical, structural and magnetic properties of pure and doped 1*T*-TaS_2. *Phil. Mag. B* **39**, 229–244 (1979).
17. D. C. Licciardello, D. J. Thouless, Constancy of minimum metallic conductivity in two dimensions. *Phys. Rev. Lett.* **35**, 1475–1478 (1975).
18. S. G. Lemay, R. E. Thorne, Y. Li, J. D. Brock, Temporally ordered collective creep and dynamic transition in the charge-density-wave conductor $NbSe_3$. *Phys. Rev. Lett.* **83**, 2793–2796 (1999).
19. S. V. Zaitsev-Zotov, V. E. Minakova, Evidence of collective charge transport in the Ohmic regime of *o*-TaS_3 in the charge-density-wave state by a photoconduction study. *Phys. Rev. Lett.* **97**, 266404 (2006).
20. N. Ogawa, A. Shiraga, R. Kondo, S. Kagoshima, K. Miyano, Photocontrol of dynamic phase transition in the charge-density wave material $K_{0.3}MoO_3$. *Phys. Rev. Lett.* **87**, 256401 (2001).
21. A. Tomeljak, H. Schäfer, D. Städter, M. Beyer, K. Biljakovic, J. Demsar, Dynamics of photoinduced charge-density-wave to metal phase transition in $K_{0.3}MoO_3$. *Phys. Rev. Lett.* **102**, 066404 (2009).
22. N. M. Gabor, J. C. W. Song, Q. Ma, N. L. Nair, T. Taychatanapat, K. Watanabe, T. Taniguchi, L. S. Levitov, P. Jarillo-Herrero, Hot carrier–assisted intrinsic photoresponse in graphene. *Science* **334**, 648–652 (2011).
23. J. Yao, J. Shao, Y. Wang, Z. Zhao, G. Yang, Ultra-broadband and high response of the Bi_2Te_3–Si heterojunction and its application as a photodetector at room temperature in harsh working environments. *Nanoscale* **7**, 12535–12541 (2015).
24. Y. Y. Niu, D. Wu, Y. Q. Su, H. Zhu, B. Wang, Y. X. Wang, Z. R. Zhao, P. Zheng, J. S. Niu, H. B. Zhou, J. Wei, N. L. Wang, Uncooled $EuSbTe_3$ photodetector highly sensitive from ultraviolet to terahertz frequencies. *2D Mater.* **5**, 011008 (2018).
25. L. Liu, J. Niu, H. Guo, J. F. Wei, D. L. Li, J. F. Feng, X. F. Han, J. M. D. Coey, X.-G. Zhang, Spin-flip noise due to nonequilibrium spin accumulation. *Phys. Rev. B* **93**, 180401(R) (2016).
26. A. Rogalski, Infrared detectors: Status and trends. *Prog. Quantum Electron.* **27**, 59–210 (2003).
27. C. Zhong, F. Huang, Y. Cao, D. Moses, A. J. Heeger, Role of localized states on carrier transport in bulk heterojunction materials comprised of organic small molecule donors. *Adv. Mater.* **26**, 2341–2345 (2014).
28. D. N. Basov, R. D. Averitt, D. Hsieh, Towards properties on demand in quantum materials. *Nat. Mater.* **16**, 1077–1088 (2017).
29. K. Nasu, *Photoinduced Phase Transitions* (World Scientific Publishing Co. Inc., 2004).
30. C. C. Homes, M. Reedyk, D. A. Crandles, T. Timusk, Technique for measuring the reflectance of irregular, submillimeter-sized samples. *Appl. Opt.* **32**, 2976–2983 (1993).
31. L. V. Gasparov, K. G. Brown, A. C. Wint, D. B. Tanner, H. Berger, G. Margaritondo, R. Gaál, L. Forró, Phonon anomaly at the charge ordering transition in 1T-TaS_2. *Phys. Rev. B* **66**, 094301 (2002).
32. M. D. Núñez-Regueiro, J. M. Lopez-Castillo, C. Ayache, Thermal conductivity of 1*T*-TaS_2 and 2*H*-$TaSe_2$. *Phys. Rev. Lett.* **55**, 1931–1934 (1985).
33. X. Deng, Y. Wang, Z. Zhao, Z. Chen, J.-L. Sun, Terahertz-induced photothermoelectric response in graphene-metal contact structures. *J. Phys. D Appl. Phys.* **49**, 425101 (2016).
34. M. Mittendorff, S. Winnerl, J. Kamann, J. Eroms, D. Weiss, H. Schneider, M. Helm, Ultrafast graphene-based broadband THz detector. *Appl. Phys. Lett.* **103**, 021113 (2013).
35. D. Spirito, D. Coquillat, S. L. De Bonis, A. Lombardo, M. Bruna, A. C. Ferrari, V. Pellegrini, A. Tredicucci, W. Knap, M. S. Vitiello, High performance bilayer-graphene terahertz detectors. *Appl. Phys. Lett.* **104**, 061111 (2014).
36. L. Vicarelli, M. S. Vitiello, D. Coquillat, A. Lombardo, A. C. Ferrari, W. Knap, M. Polini, V. Pellegrini, A. Tredicucci, Graphene field-effect transistors as room-temperature terahertz detectors. *Nat. Mater.* **11**, 865–871 (2012).
37. X. Cai, A. B. Sushkov, R. J. Suess, M. M. Jadidi, G. S. Jenkins, L. O. Nyakiti, R. L. Myers-Ward, S. Li, J. Yan, D. K. Gaskill, T. E. Murphy, H. D. Drew, M. S. Fuhrer, Sensitive room-temperature terahertz detection via the photothermoelectric effect in graphene. *Nat. Nanotechnol.* **9**, 814–819 (2014).
38. A. V. Muraviev, S. L. Rumyantsev, G. Liu,A. A. Balandin, W. Knap, M. S. Shur, Plasmonic and bolometric terahertz detection by graphene field-effect transistor. *Appl. Phys. Lett.* **103**, 181114 (2013).

Acknowledgments: We acknowledge fruitful discussions with W. He, J. Yuan, M. Y. Zhang, L. Y. Shi, and T. Lin. **Funding:** This work was supported by the National Science Foundation of China (nos. 11327806 and GZ1123) and the National Key Research and Development Program of China (nos. 2016YA0300902 and 2017YFA0302904). **Author contributions:** N.W., D.W., and Y.M. designed the experiments. D.W., Y.M., Y.N., Q.L., T.D., and S.Z. performed crystal

growth, device fabrication, and electrical property measurements. J.N., H.Z., and J.W. performed noise analysis. D.W., Y.N., Y.W., Z.Z., T.D., and Q.L. performed photoresponse experiments and analyzed the data. D.W. wrote the manuscript, with contributions from all the authors. N.W. and D.W. conceived the project. All authors have approved the final version of the manuscript. **Competing interests:** The authors declare that they have no competing interests. **Data and materials availability:** All data needed to evaluate the conclusions in the paper are present in the paper and/or the Supplementary Materials. Additional data related to this paper may be requested from the authors.

Submitted 6 July 2017
Accepted 22 June 2018
Published 3 August 2018
10.1126/sciadv.aao3057

Citation: D. Wu, Y. Ma, Y. Niu, Q. Liu, T. Dong, S. Zhang, J. Niu, H. Zhou, J. Wei, Y. Wang, Z. Zhao, N. Wang, Ultrabroadband photosensitivity from visible to terahertz at room temperature. *Sci. Adv.* **4**, eaao3057 (2018).

Science Advances

Ultrabroadband photosensitivity from visible to terahertz at room temperature

Dong Wu, Yongchang Ma, Yingying Niu, Qiaomei Liu, Tao Dong, Sijie Zhang, Jiasen Niu, Huibin Zhou, Jian Wei, Yingxin Wang, Ziran Zhao and Nanlin Wang

Sci Adv **4** (8), eaao3057.
DOI: 10.1126/sciadv.aao3057